The mass profile and dynamical status of the $z \sim 0.8$ galaxy cluster LCDCS 0504 ⋆

L. Guennou[1,2], A. Biviano[3,4], C. Adami[2], M. Limousin[2], G.B. Lima Neto[5], G.A. Mamon[4], M.P. Ulmer[6], R. Gavazzi[4], E.S. Cypriano[5], F. Durret[4], D. Clowe[7], V. LeBrun[2], S. Allam[8,9], S. Basa[2], C. Benoist[10], A. Cappi[11,10], C. Halliday[12], O. Ilbert[2], D. Johnston[8], E. Jullo[2], D. Just[13,14], J.M. Kubo[8], I. Márquez[15], P. Marshall[16], N. Martinet[4], S. Maurogordato[10], A. Mazure[2], K.J. Murphy[7], H. Plana[17], F. Rostagni[10], D. Russeil[2], M. Schirmer[18,19], T. Schrabback[20], E. Slezak[10], D. Tucker[8], D. Zaritsky[13], and B. Ziegler[21]

1 Astrophysics and Cosmology Research Unit, University of KwaZulu-Natal, Durban, 4041, South Africa
2 Aix Marseille Université, CNRS, LAM (Laboratoire d'Astrophysique de Marseille) UMR 7326, 13388, Marseille, France
3 INAF/Osservatorio Astronomico di Trieste, via Tiepolo 11, 34143 Trieste, Italy
4 Institut d'Astrophysique de Paris (UMR7095: CNRS & UPMC), 98 bis Bd Arago, F-75014, Paris, France
5 Departamento de Astronomia, Instituto de Astronomia Geofìsica e Ciências Atmosfèricas, Universidade de São Paulo, Rua do Matão 1226, 05508-900 São Paulo, Brazil
6 Department Physics & Astronomy & Center for Interdisciplinary Exploration and Research in Astrophysics (CIERA), Northwestern University, Evanston, IL 60208-2900, USA
7 Department of Physics and Astronomy, Ohio University, 251B Clippinger Lab, Athens, OH 45701, USA
8 Fermi National Accelerator Laboratory, P.O. Box 500, Batavia, IL 60510, USA
9 CSC/STSCi, 3700 San Martin Dr., Baltimore, MD 21218, USA
10 OCA, Cassiopée, Boulevard de l'Observatoire, BP 4229, 06304 Nice Cedex 4, France
11 INAF/Osservatorio Astronomico di Bologna, via Ranzani 1, 40127 Bologna, Italy
12 23, rue d'Yerres, 91230 Montgeron, France
13 Steward Observatory, University of Arizona, 933 N. Cherry Ave. Tucson, AZ 85721, USA
14 Department of Astronomy & Astrophysics, University of Toronto, 50 St George Street Toronto, Ontario M5S 3H4, Canada
15 Instituto de Astrofísica de Andalucía (CSIC), Glorieta de la Astronomía s/n, 18008, Granada, Spain
16 Kavli Institute for Particle Astrophysics and Cosmology, Stanford University, 2575 Sand Hill Rd., Menlo Park, CA 94025, USA
17 Laboratório de Astrofísica Teórica e Observacional, Universidade Estadual de Santa Cruz, Ilhéus, Brazil
18 Gemini Observatory, Casilla 603, La Serena, Chile
19 Argelander-Institut für Astronomie, Universitët Bonn, Auf dem Hügel 71, 53121, Bonn, Germany
20 Physics Department, University of California, Santa Barbara, CA 93601, USA
21 University of Vienna, Department of Astrophysics, Türkenschanzstr. 17, 1180 Wien, Austria

Accepted . Received ; Draft printed: July 22, 2014

ABSTRACT

Context. Constraints on the mass distribution in high-redshift clusters of galaxies are not currently very strong.
Aims. We aim to constrain the mass profile, $M(r)$, and dynamical status of the $z \sim 0.8$ LCDCS 0504 cluster of galaxies characterized by prominent giant gravitational arcs near its center.
Methods. Our analysis is based on deep X-ray, optical, and infrared imaging, as well as optical spectroscopy, collected with various instruments, complemented with archival data. We model the mass distribution of the cluster with three different mass density profiles, whose parameters are constrained by the strong lensing features of the inner cluster region, by the X-ray emission from the intra-cluster medium, and by the kinematics of 71 cluster members.
Results. We obtain consistent $M(r)$ determinations from three methods based on kinematics (dispersion-kurtosis, caustics and MAMPOSSt), out to the cluster virial radius, $\simeq 1.3$ Mpc and beyond. The mass profile inferred by the strong lensing analysis in the central cluster region is slightly above, but still consistent with, the kinematics estimate. On the other hand, the X-ray based $M(r)$ is significantly below both the kinematics and strong lensing estimates. Theoretical predictions from ΛCDM cosmology for the concentration–mass relation are in agreement with our observational results, when taking into account the uncertainties in both the observational and theoretical estimates. There appears to be a central deficit in the intra-cluster gas mass fraction compared to nearby clusters.
Conclusions. Despite the relaxed appearance of this cluster, the determinations of its mass profile by different probes show substantial discrepancies, the origin of which remains to be determined. The extension of a similar dynamical analysis to other clusters of the DAFT/FADA survey with multi-wavelength data of sufficient quality, will allow to shed light on the possible systematics that affect the determination of mass profiles of high-z clusters, possibly related to our incomplete understanding of intracluster baryon physics.

Key words. Galaxies: clusters: general, Galaxies: kinematics and dynamics

1. Introduction

The study and characterization of the internal dynamics of galaxy clusters is an important way to understand their evolutionary history, which is itself related to the evolutionary history of the universe. The most classical way to characterize the dynamics of clusters is through the analysis of the projected phase space distribution of their member galaxies, e.g. via methods based on the Jeans equation (Binney & Tremaine 1987), such as the Dispersion-Kurtosis (Łokas & Mamon 2003), distribution-function (Wojtak et al. 2009) and MAMPOSSt (Mamon et al. 2013) methods, or the Caustic method calibrated on numerical simulations (Diaferio & Geller 1997). All these methods assume spherical symmetry and most of them (except the Caustic method) also assume dynamical relaxation of the cluster. These methods have been applied to several nearby (and massive) clusters of galaxies (see Kent & Gunn 1982; van der Marel et al. 2000; Biviano & Girardi 2003; Łokas & Mamon 2003; Biviano & Katgert 2004; Katgert et al. 2004; Biviano 2006; Łokas et al. 2006; Wojtak & Łokas 2010).

Given that clusters formed relatively recently according to the hierarchical scenario of structure evolution in the universe (e.g. Borgani & Guzzo 2001), accretion of matter from the surrounding field, in the form of galaxy groups, complicate their internal structure. Detection of secondary structures, or substructures, in clusters is obtained using other methods, either based on the projected distributions of cluster galaxies (e.g. Dressler & Shectman 1988; Escalera et al. 1994; Biviano et al. 1996; Serna & Gerbal 1996; Barrena et al. 2002; Girardi & Biviano 2002; Ramella et al. 2007) or on X-ray data for the intra-cluster gas (Briel et al. 1991; Mohr et al. 1993; Neumann et al. 2001; O'Hara et al. 2004; Pratt et al. 2005; Böhringer et al. 2010). Detection and characterization of these substructures is a direct way to constrain the cluster building history (e.g. Adami et al. 2005, and references therein).

These last years, the characterization of the mass distribution and substructures of galaxy clusters has been made possible by investigating deep and high quality data that enable the measurement of weak lensing signal and the detection of strong gravitationally lensed features (e.g. Cypriano et al. 2004; Markevitch et al. 2004; Bardeau et al. 2005; Jee et al. 2005; Coe et al. 2010; Leonard et al. 2011). It is still relatively uncommon to see cluster dynamical studies based simultaneously on the Jeans analysis, and on the X-ray and lensing data, especially for high redshift clusters. This is due to the extreme difficulty in obtaining both deep and high resolution X-ray imaging, deep optical and infrared imaging, and faint galaxy spectroscopy. As a consequence, our information on the internal structure and dynamics of distant clusters is still relatively limited.

In this paper, we perform a detailed study of the internal structure and dynamics of the rich cluster LCDCS 0504 at redshft $z = 0.7943$, also known as Cl J1216.8-1201 (Nelson et al. 2001), using simultaneously spectroscopic optical data for cluster galaxies, as well as X-ray and strong lensing (SL, hereafter) data. This cluster is part of the DAFT/FADA survey (Guennou et al. 2010) and the analysis presented here is a proof of concept for similar analysis to be performed on other clusters of the DAFT/FADA sample.

In Sect. 2 we present our data-set. Our SL determination of the cluster mass distribution is described in Sect. 3. In Sect. 4 we use the X-ray emission from the hot intra-cluster medium (ICM) to constrain the cluster mass profile. This is also determined using galaxies as tracers in Sect. 5. We compare the different mass profile determinations in Sect. 6. In Sect. 7 we analyse the cluster hot gas mass fraction. We discuss our results in Sect. 8, where we also draw our conclusions.

Throughout this paper we adopt $H_0 = 70$ km s^{-1} Mpc^{-1}, $\Omega_m = 0.3$, $\Omega_\Lambda = 0.7$. In this cosmology, 1 arcmin corresponds to 449 kpc at the cluster redshift.

Table 1. Available data for the LCDCS 0504 cluster.

	Archival data	DAFT/FADA data
Optical imaging	$VRIz$ (VLT/FORS2) $F814W$ (HST/ACS)	B (Blanco/MOSAIC)
IR imaging	Spitzer/IRAC1 and 2	
Optical spectroscopy	VLT/FORS2	Gemini/GMOS
X-ray imaging	XMM-Newton (PN/MOS1/MOS2)	

2. The data

The DAFT/FADA survey is described at http://cesam.oamp.fr/DAFT/. Here we focus on the description of the data available for LCDCS 0504, summarized in Table 1.

2.1. Optical and near-infrared imaging

We refer to Guennou et al. (2010) for a complete description of the optical and infrared imaging data and for the evaluation of photometric redshifts, $z_{\rm p}$. These photometric redshifts are characterized by typical uncertainties lower than 0.1 up to z ~1.5 for

Send offprint requests to: L. Guennou, guennou@ukzn.ac.za

⋆ Based on XMM-Newton archive data and on data retrieved from the NASA/IPAC Extragalactic Database (NED) which is operated by the Jet Propulsion Laboratory, California Institute of Technology, under contract with the National Aeronautics and Space Administration. Also based on observations made with the FORS2 multi-object spectrograph mounted on the Antu VLT telescope at ESO-Paranal Observatory (programme 175.A-0706(B)). Also based on observations obtained at the Gemini Observatory, which is operated by the Association of Universities for Research in Astronomy, Inc., under a cooperative agreement with the NSF on behalf of the Gemini partnership: the National Science Foundation (United States), the Science and Technology Facilities Council (United Kingdom), the National Research Council (Canada), CONICYT (Chile), the Australian Research Council (Australia), Ministério da Ciência, Tecnologia e Inovação (Brazil) and Ministerio de Ciencia, Tecnología e Inovación Productiva (Argentina). Finally, this research has made use of the VizieR catalog access tool, CDS, Strasbourg, France. Also based on observations made with the NASA/ESA Hubble Space Telescope, obtained from the data archive at the Space Telescope Science Institute. STScI is operated by the Association of Universities for Research in Astronomy, Inc. under NASA contract NAS 5-26555. Also based on visiting astronomer observations, at Cerro Tololo Inter-American Observatory, National Optical Astronomy Observatory, which is operated by the Association of Universities for Research in Astronomy, under contract with the National Science Foundation. This work has been carried out thanks to the support of the Labex OCEVU (ANR-11-LABX-0060) and the A*MIDEX (ANR-11-IDEX-0001-02) funded by the "Investments for the Future" French government program managed by the French National Research Agency (ANR)

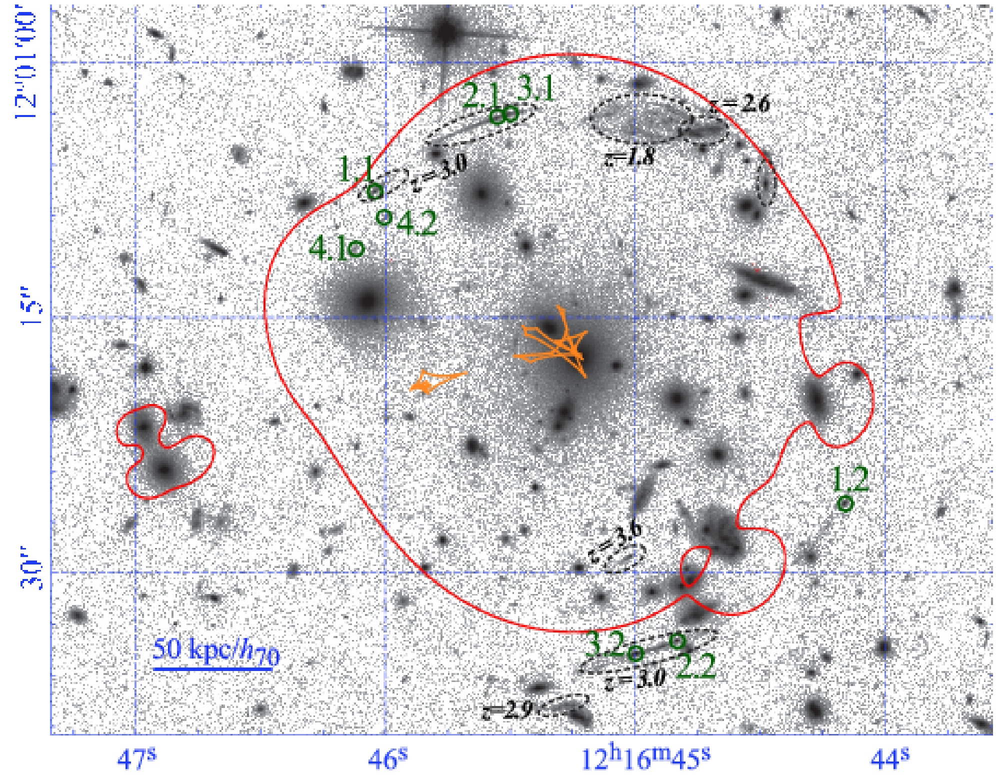

Fig. 1. HST image of the core of LCDCS 0504. The size of the field is 38×34 arcsec^2, corresponding to 285 × 255 kpc^2 at z = 0.794. Multiple imaged systems used in this work are labeled. From the best fit strong lensing model, we draw in red the tangential critical curve at z=3 and the corresponding caustic lines in orange

galaxies brighter than $F814W$ = 22.5, or up to z ∼1 for galaxies brighter than $F814W$ = 24. The photometric redshifts are used here to define cluster membership in the absence of spectroscopic information (see Sect. 5.2).

2.2. Optical spectroscopy

We collected 116 galaxy redshifts from the NED database, originally from Halliday et al. (2004), obtained with VLT/FORS2 observations in a 5 arcmin radius around the cluster center. The average error on these redshift measurements corresponds to 90 km s^{-1} in velocity. This sample of spectroscopic redshifts is limited to $z \leq 1.1$. The magnitude distribution of the spectroscopic sample peaks at an I-band magnitude of 22, and is limited to $I \leq 24$. We were awarded 6 hours of Gemini/GMOS time (program GS2011A-014) to observe spectroscopically the three brightest giant arcs. The initial spectral resolution was 150, but was degraded to 10 Å/px in order to increase the S/N. This theoretically provides a redshift uncertainty of the order of 0.0015 (i.e. ∼ 500 km s^{-1}), corresponding to an uncertainty of 1 pixel in the line location. Following the identification labels of the observed objects in Fig. 1, we measured z ∼ 2.988 for the object 1.3/1.4, z ∼ 3.005 for the object 1.2, and z ∼ 3.009 for the object 1.1. Assuming that the 3 objects are multiple images of a single background object, we stacked the 3 spectra together (see Fig. 2) and measured a redshift of 3.005 for the stacked spectrum. From the best fit strong lensing model, we draw in red the tangential critical curve at z=3 (location where the amplification diverges) and in orange the caustic lines (which are generated by de-lensing the critical lines in the source plane)

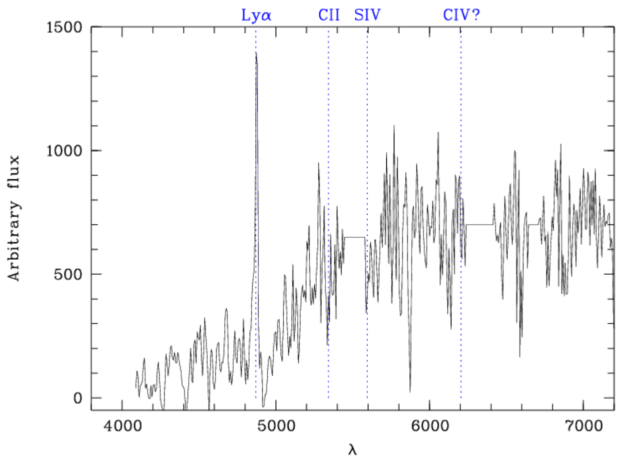

Fig. 2. Summed spectrum of arcs 1.1, 1.2, and 1.3. The best redshift is 3.005.

Remaining slits were put on galaxies along the cluster line-of-sight (los). For a cross check and for comparison, we included 13 galaxies in this sample with redshifts already available in the literature. Combined with publicly available data, our final sample contains 137 galaxies with redshifts, all with $z \leq 1.15$ and $I \leq 24.5$ (the I magnitude distribution of our sample peaks at I = 22.5). Coordinates and redshifts for this sample are given in Table 2 (available electronically only). Among the 13 galaxies in common between our GMOS measurements and the literature, only one (with a low S/N in the GMOS data) showed discrepant redshift measurements (0.6605 in GMOS vs. 0.7220 in the liter-

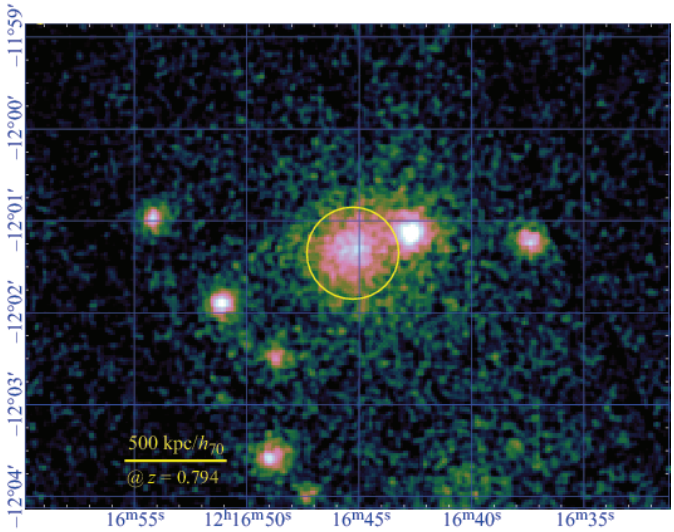

Fig. 3. XMM-Newton image using all available data. The cluster is shown inside the yellow central circle of radius equal to 30″. The other visible X-ray sources are point source AGNs.

ature). The discrepancy probably arises from a different identification of a spectral feature that we attributed to an Hδ absorption line, while it was attributed to the Ca H line in the literature. Our redshift measurements for the other 12 galaxies are in very good agreement with the previous measurements, with a mean difference of -0.0003 ± 0.0013. This uncertainty is in agreement with the expected uncertainty of our GMOS measurements. We adopt 390 km s^{-1} as the average velocity error for these data.

2.3. X-ray data

We have downloaded the publicly available XMM-*Newton* observations of LCDC 0504: ID 0143210801, observed in 07/2003, PI D. Zaritsky, and ID 0651770201, observed in 12/2010, PI B. Maughan. Both observations were reprocessed with SAS 12[1], using the latest available calibration files. High background (flares) time intervals were removed with a σ-clip method using the light-curve of the 2.0–12.0 keV band.

The final exposure times, after flare subtraction, are, for the 2003 observation: 22.71, 22.34, and 18.36 ks for the MOS1, MOS2, and pn, respectively. For the 2010 observation we have 59.96, 63.83, and 27.89 ks for the MOS1, MOS2, and pn, respectively.

For each observation and detector we have produced exposure-map corrected images in the 0.3–7.0 keV band. All these images were merged together using the task imcombine/IRAF, and the result is shown in Fig. 3.

3. Mass profile from strong lensing

Motivated by the spectroscopy of the blue lensed features in the cluster core (Section 2.2) and after inspection of both the high resolution HST/ACS image and the ground based B, R, I images, we propose that objects 1 through 3 in Table 3 are the result of a *single* background galaxy at $z = 3.0$ is being strongly lensed by Cl 1216. We observe two images of this background source. Each image is resolved into three sub-images, which correspond to different sub-structures of the background source. They are labelled systems 1, 2 and 3 (Fig. 1). We also conjugate two close images, forming system 4. Having no redshift information for this system, we let its redshift free during the optimization.

Beginning with this set as constraints, we modeled the cluster mass distribution using a dual Pseudo Isothermal Elliptical Mass Distribution (dPIE, hereafter; Limousin et al. 2005; Elíasdóttir et al. 2007). The dPIE model is based on the Pseudo Isothermal mass profile, characterized by the 3D mass profile[2]

$$M(r) = 2\,\frac{s\,\sigma_0^2}{G\,(s-a)}\left[s\,\tan^{-1}\left(\frac{r}{s}\right) - a\,\tan^{-1}\left(\frac{r}{a}\right)\right], \tag{1}$$

provides a 3D density profile:

$$\rho(r) = \frac{\sigma_0^2}{2\pi G}\,\frac{s\,(a+s)}{(r^2+a^2)\,(r^2+s^2)}, \tag{2}$$

where G is the gravitational constant, r is the 3D clustercentric radial distance, a the core radius, s the scale radius, σ_0 the central velocity dispersion. This profile is not isothermal (slope −2) at all radii but only in the intermediate radial range $a \le r \le s$. This $M(r)$ corresponds to the projected mass density profile,

$$\Sigma(R) = \frac{s\,\sigma_0^2}{4G\,(s-a)}\,[(R^2+a^2)^{-1/2} - (R^2+s^2)^{-1/2}], \tag{3}$$

where R is the 2D projected clustercentric radial distance. The dPIE is obtained by replacing R with

$$\widetilde{R}^2 = \frac{X^2}{(1+\epsilon)^2} + \frac{Y^2}{(1-\epsilon)^2}, \tag{4}$$

where the ellipticity is defined as $\epsilon \equiv (A-B)/(A+B)$, with A, B the semi-major and, respectively, semi-minor axis, and X, Y are the spatial coordinates along the major, and, respectively, minor axes. There are 6 free parameters in the dPIE model, the two coordinates of the cluster center, the ellipticity, the orientation angle, the velocity dispersion, and the core and scale radii.

We rely on the dPIE model results to identify and search for other gravitational arcs. We note, though, that we could not distinguish between the dPIE model and a NFW model (Navarro et al. 1997) with our SL analysis, given the uncertainties. However, we prefer using a dPIE profile since the parameters can be constrained by our SL analysis, whereas the NFW profile (in particular the scale radius) is out of reach of the SL constraints (but not out of reach of modeling based on kinematics data, see Sect. 5).

We fix the scale radius s to 1 Mpc since it cannot be constrained by our data. Furthermore, after some tests, we figured out that the core radius was constrained to be smaller than ∼ 5″, i.e. smaller than the range where multiply imaged systems are found. We fix it to 2″. Note that with this choice of parametrization, the cluster is modelled using a mass profile which is close to isothermal. Given the circular aspect of this cluster, we impose its position to be within ± 5″ from the BCG galaxy. Together with the ellipticity and the position angle of the mass distribution, this gives 5 parameters to be optimized. On top of this smooth component, we include perturbations from the brightest cluster members located close (i.e. less that ∼ 5″) to the multiply imaged systems. This gives 11 individual galaxies. Following earlier works (e.g. Limousin et al. 2007b), we describe these perturbers using a dPIE profile, whose geometrical parameters

[1] Science Analysis System from the XMM-Newton team, http://xmm.esac.esa.int/sas/current/sas_news.shtml

[2] This is the total mass enclosed within a radius r, sometimes written as $M(< r)$ in the literature.

Table 3. Multiply imaged systems for the SL analysis.

ID	R.A. (J2000)	Decl. (J2000)	$z_{\rm spec}$	$z_{\rm model}$
1.1	184.19186	−12.01878	3.0	—
1.2	184.18402	−12.02390	3.0	—
2.1	184.18985	−12.01758	3.0	—
2.2	184.18683	−12.02611	3.0	—
3.1	184.18965	−12.01752	3.0	—
3.2	184.18752	−12.02630	3.0	—
4.1	184.19216	−12.01974	assumed	2.3±0.5
4.2	184.19171	−12.01922	assumed	2.3±0.5

Table 4. dPIE mass model parameters.

R.A. (arcsec)	−1.1±0.8
Decl. (arcsec)	$0.5^{+0.9}_{-2.1}$
ϵ	0.07±0.04
orientation angle (degrees)	91±8
σ_0 (km s^{-1})	839±14
a (kpc)	[14]
s (kpc)	[1 000]

Notes. Coordinates are given in arc-seconds with respect to the cD galaxy located at $\alpha = 184.^{\circ}18845$, $\delta = -12.^{\circ}021472$. Error bars correspond to 1σ confidence level as inferred from the Monte Carlo Markov Chain optimization.

(position, ellipticity, position angle) are set to the one measured from their light distribution. Their core radius is set to 0, and their scale radius to 45 kpc, which describe compact dark matter haloes, as expected for central cluster galaxies within a tidal stripping scenario (Limousin et al. 2007a). Their velocity dispersion is scaled with their luminosity (see Limousin et al. 2007, ApJ for more details). Therefore, the perturbers are modeled using one extra parameter. Using the 8 constraints provided by the multiply imaged systems, we optimize the mass model in the image plane, using the Lenstool[3] software (Jullo et al. 2007). We find that this simple unimodal model is able to reproduce accurately the multiply imaged systems, with an RMS of 0.15″ (image plane).

The mass model predicts a third central image for the strongly lensed background galaxy at $z = 3.0$, predicted to be more than 5 magnitudes fainter than the main images. System 4 is predicted to be at $z = 2.4 \pm 0.4$. Finally, we have not been able to reliably find the counterimage of the blue feature located at $\alpha = 184.^{\circ}18761, \delta = -12.^{\circ}024721$ (yellow circle on Fig. 1). One possibility is that it is singly imaged. In that case, its redshift should be smaller than 1.35.

4. Mass profile from X-ray data

We have produced a surface brightness image of LCDCS 0504 by merging all the individual detectors (MOS1, MOS2, and pn from both 2003 and 2010 exposures) exposure-map corrected images. We then fitted the X-ray surface-brightness profile of LCDCS 0504 by a 2D, elliptical β-model[4]

$$I(R) = I_0 \left[1 + \left(\frac{R}{r_c} \right)^2 \right]^{1/2 - 3\beta_X} + B\,, \quad (5)$$

with best-fit values $\beta_X = 0.52 \pm 0.06$ and $r_c = (113 \pm 19)$ kpc, see Fig. 4.

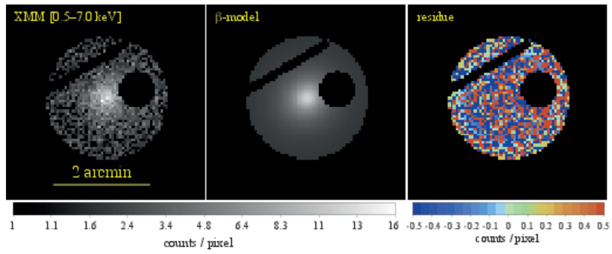

Fig. 4. 2D surface brightness fit. Left: LCDCS 0504 image in the [0.5-7.0 keV] band with point sources and artefacts (CCD gap) masked out. Middle: best-fit β-model (see text for details) shown with the same color coding of the original image. Right: residuals, data minus best-fit model. No apparent structure is seen on the residual image.

The fit with a β-model is good, and this suggests the cluster is not cool-core, as a cuspy density profile is usually observed in cool-core clusters. In non cool-core clusters the temperature is usually isothermal inside r_{500}. We therefore opt for using a single mean temperature for the dynamical modeling. In any case, the data are too sparse to determine such a significant non-isothermal nature of the gas so as to change our conclusions. It is not feasible to obtain a meaningful radial temperature profile with the $\sim$ 5800 net counts (i.e., background subtracted and masking the bright point source to the West) resulting from the LCDCS0504 X-ray flux of $(1.0 \pm 0.4)\, 10^{-13}$ erg s^{-1} cm^{-2}, inside 1 arcmin in the [0.5–10.0] keV band.

A spectral analysis was used to compute the central gas density, as well as its temperature, that was estimated with XSPEC v12, from HEASARC[5]. The X-ray spectrum was extracted within a region of radius 1 arcmin (point sources were masked) and modeled as an emission from a single temperature plasma (mekal model; Kaastra & Mewe 1993; Liedahl et al. 1995). We have fitted simultaneously all the spectral data, MOS1, MOS2 and pn from both 2003 and 2010 observations. The photoelectric absorption – mainly due to Galactic neutral hydrogen – was computed using the cross-sections given by Balucinska-Church & McCammon (1992), available in XSPEC. Metal abundances (metallicities) were scaled to the Anders & Grevesse (1989) solar values.

For the MOS spectra, we restricted our fit to the interval 0.5–7.0 keV, while for the pn data, we used the 0.7–7.0 keV. We kept the hydrogen column density fixed for the fit at the Galactic value, $N_{\rm H} = 3.26 \times 10^{22}$ cm^{-2}, in the direction of LCDCS 0504 (LAB survey, Kalberla et al. 2005).

Our best fit, shown in Fig. 5 had a reduced $\chi^2 = 0.867$ for 491 degrees of freedom with the following free parameters: $kT = 5.1^{+0.66}_{-0.55}$ keV and $Z = 0.23^{+0.17}_{-0.15} Z_{\odot}$. Inside a radius of 1 arcmin the fitted spectral model implies a bolometric X-ray luminosity of $L_X = (2.90 \pm 0.18) \times 10^{44}$ erg s^{-1}. Our spectral fit agrees quite well with the thorough analysis done by Johnson et al. (2006), who used only the first, shallower XMM observation.

[3] http://www.oamp.fr/cosmology/lenstool/

[4] We use β_X for the parameter of the model to distinguish it from the kinematics β, see eq. 9. (Cavaliere & Fusco-Femiano 1976), with a flat background added to it:

[5] http://heasarc.gsfc.nasa.gov/

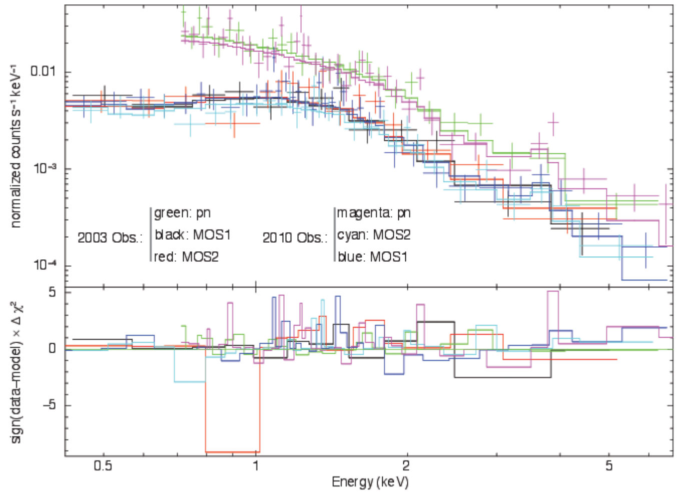

Fig. 5. Best-fit absorbed MEKAL model. Top: All detectors from both XMM-*Newton* observation are fitted simultaneously, as described in the text. Bottom: Plot of the residual contribution to the χ^2 per energy bin of the best fit spectrum.

Assuming an isothermal plasma, the 3D deprojection of Eq. (5) is:

$$n(r) = n_0 \left[1 + \left(\frac{r}{r_c}\right)^2\right]^{-3\beta_X/2} , \tag{6}$$

where n_0 is the central particle number density in units of cm^{-3} and the radii r and r_c are given in kpc. The central density was obtained by normalizing the X-ray flux measured with the expected bremsstrahlung flux from an isothermal β-model distribution. From the spectral analysis we obtain $n_0 = (6.5 \pm 0.7) \times 10^{-3}$ cm^{-3}.

The total mass profile, assuming isothermal hydrostatic equilibrium and a spherical β-model, is given by:

$$M(r) = 6.68 \times 10^{10} \frac{\beta_X kT}{\mu r_c^2} \frac{r^3}{1 + r^2/r_c^2} M_\odot , \tag{7}$$

where $\mu = 0.6$, kT is in keV, while r and r_c are in kpc. The values of r_{200} and r_{-2} corresponding to this mass profile are given in Table 5. Note that also in this case, as for the SL determination, the value of r_{200} is based on an extrapolation of the mass profile beyond the region where it is constrained. The total density profile corresponding to the mass profile of equation (7) is

$$\rho(r) \propto \frac{r^2 + 3r_c^2}{(r^2 + r_c^2)^2} . \tag{8}$$

5. Mass profile from kinematics

Here, we use the projected phase space distribution of cluster galaxies to constrain the mass distribution of the cluster. We adopted three methods of deriving a mass model based solely on the optical data, two based on the Jeans equation (e.g. Binney & Tremaine 1987), and one based on the Caustic method (Diaferio & Geller 1997; Diaferio 1999). The methods based on the Jeans equation are "Dispersion-Kurtosis" (Łokas & Mamon 2003, DK hereafter), and "MAMPOSSt" (Mamon et al. 2013). All three methods assume spherical symmetry.

The DK method performs a simultaneous best-fit of the parameters of a model mass profile, $M(r)$, and of a model velocity anisotropy profile,

$$\beta(r) = 1 - \frac{\sigma_\theta^2(r) + \sigma_\phi^2(r)}{2\,\sigma_r^2(r)} = 1 - \frac{\sigma_\theta^2(r)}{\sigma_r^2(\mathrm{r})} \tag{9}$$

where $\sigma_\theta, \sigma_\phi$ are the two tangential components, and σ_r the radial component, of the velocity dispersion, and the last equivalence is obtained in the case of spherical symmetry. The fit is done by minimizing the summed χ^2 of the fits to the binned line-of-sight velocity dispersion profile, $\sigma_{\mathrm{los}}(R)$, and to the binned line-of-sight kurtosis profile, $K(R)$, corrected for the known statistical bias using the expression in DeCarlo (1997). Using these two profiles rather than just one allows to partially break the degeneracy between the $M(r)$ and $\beta(r)$ parameters. A limitation of this method is that it assumes that $\beta(r)$ is constant with radius.

The MAMPOSSt method, like the DK method, determines the best-fit parameters of model $M(r)$ and $\beta(r)$, but unlike the DK method it requires no binning of the observables, since it performs a maximum likelihood fit of the full projected phase space distribution of cluster members. Unlike[6] the DK method, it has no limitation on the choice of the $\beta(r)$ model. It must however assume a shape for the 3D velocity distribution, and this is taken to be Gaussian in our analysis.

Both the DK and MAMPOSSt methods assume the cluster to be in dynamical equilibrium, so their domain of application is limited to the virial region of the cluster. The Caustic method drops this requirement, and therefore can be used to determine $M(r)$ also outside the virial region. However, the Caustic method is less accurate than DK and MAMPOSSt near the center, and tends to overestimate $M(r)$ at small radii (Serra et al. 2011). The Caustic method determines the cluster mass profile non-parametrically, from the velocity amplitude of the caustics in projected phase space, but it must assume knowledge of $\beta(r)$.

5.1. Cluster membership

Identification of the cluster members is required in the three methods, there are several methods to identify real cluster members (e.g. Wojtak et al. 2007; Mamon et al. 2013). We applied two of them here to estimate the uncertainty in the derived results. We used the method of den Hartog & Katgert (1996) and the 'Clean' method of Mamon et al. (2013). We selected these 2 approaches out of the several discussed as the former was shown by Wojtak et al. (2007) to perform marginally better than many other techniques, and the latter is a new method based on the analysis of the internal dynamics of cluster-sized halos in numerical simulations (Mamon et al. 2010).

Both methods identify real cluster members on the basis of their location in projected phase space[7], R, v_{rf}. The two methods identify the same galaxies as members of LCDCS 0504, 75 in total (see Fig. 6). Based on this sample we estimate the cluster velocity dispersion $\sigma_{\mathrm{los}} = 974^{+83}_{-76}$ km s^{-1} (biweight estimate, see Beers et al. 1990).

[6] this is no longer the case with Richardson & Fairbairn 2013

[7] For each galaxy in the cluster, R is the projected cluster-centric distance from the cD galaxy, and v_{rf} is the rest-frame velocity $v_{\mathrm{rf}} \equiv (v - v_{\mathrm{cl}})/(1 + v_{\mathrm{cl}}/c)$, where v_{cl} is the mean velocity of the cluster. This is re-defined at each new iteration of the membership selection, until convergence. The cluster center is defined to be the position of the cD galaxy.

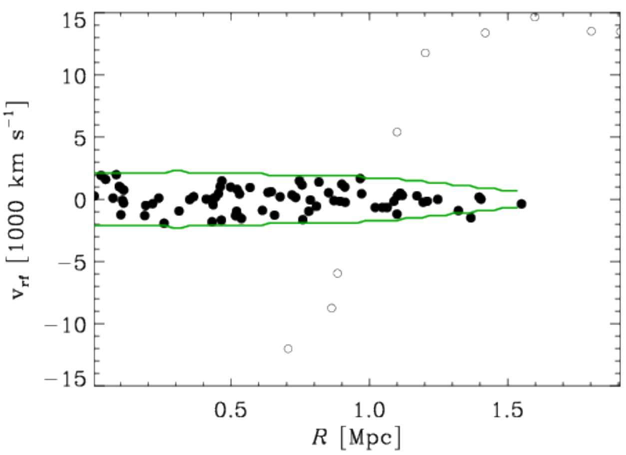

Fig. 6. The projected phase space distribution of galaxies with redshifts in the cluster region. Selected cluster members are shown as filled dots. The chosen caustic in the Caustic method is shown in green.

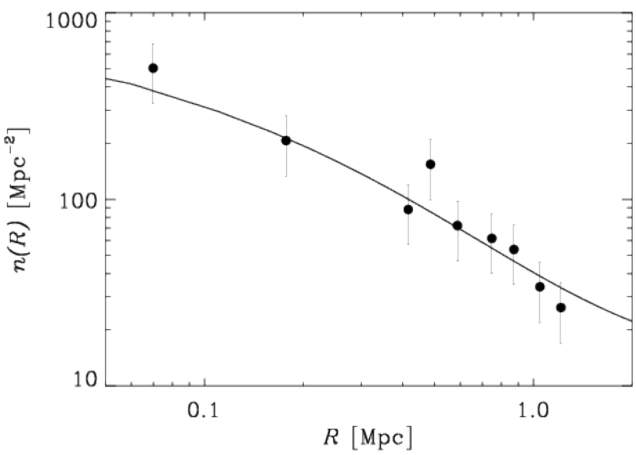

Fig. 8. The projected number density profile of $z_{\rm p}$-selected cluster members (points with 1σ error bars) and the best-fit model (projected-NFW + constant density background; solid curve). The reduced χ^2 of the fit is 0.8.

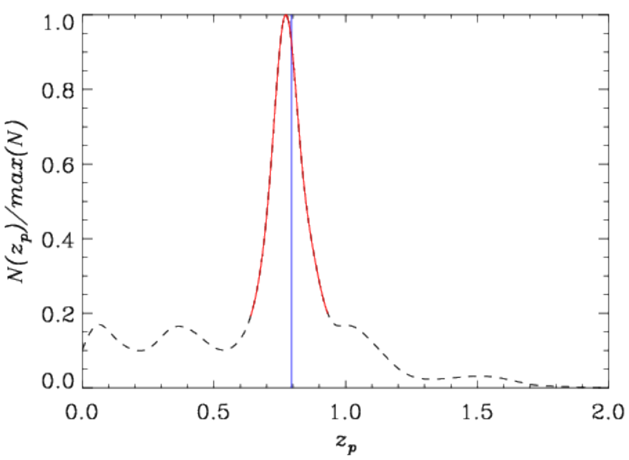

Fig. 7. The adaptive-kernel smoothed distribution of photometric redshifts for galaxies in the cluster region. The vertical (blue) line shows the average cluster redshift. The solid (red) curve shows the selected $z_{\rm p}$ range for the sample used for the determination of $n(r)$.

5.2. Galaxy number density profile

In both the DK and MAMPOSSt methods, the number density profile of the tracers of the gravitational potential, $n(r)$, needs to be estimated. This determination of $n(r)$ is the only occurrence in our dynamical analysis where completeness, or correction for incompleteness, is necessary. Since our spectroscopic sample is not complete, we use the 100% complete sample of galaxies with magnitude $F814 \leq 24$ and measured photometric redshifts, $z_{\rm p}$, for the determination of $n(r)$.

Our photometric observations fully cover the cluster only out to $\sim$ 2 arcmin from the adopted cluster center, the cD galaxy. Beyond this radius we estimate the radial geometrical completeness, $C_g(R)$, as the fractions of circular annuli covered by our observations. $C_g(R)$ drops below 50% beyond 3.3 arcmin.

We select the $z_{\rm p}$-range for defining cluster membership as follows. We smooth the $z_{\rm p}$ distribution by an adaptive kernel technique with a kernel size of 0.045, i.e. half the value of the typical uncertainty on the photometric redshifts. Larger values of the kernel size would lead to un-necessary over-smoothing of the $z_{\rm p}$ distribution, while smaller values are likely to emphasize noise-related features. We identify the main peak of the $z_{\rm p}$ distribution closest to the mean cluster redshift. We define the extremes of this peak in $z_{\rm p}$ in such a way as to avoid contamination from other peaks in the distribution, $0.64 \leq z_{\rm p} \leq 0.93$ (see Fig. 7).

We perform a maximum-likelihood fit of the spatial distribution of the 375 galaxies in the selected $z_{\rm p}$-range, weighting each galaxy by $C_g(R_i)^{-1}$, where R_i is the radial position of galaxy i, to account for geometrical incompleteness. We limit the fit of the number density profile to the radii where $C_g \geq 0.5$. The fitted model is NFW in projection (Bartelmann 1996; Łokas & Mamon 2001) to which we add a constant density background to account for interlopers in our $z_{\rm p}$ selection. Of the two free parameters of the NFW model, we are only interested in the scale radius of the galaxy number density, r_n, because the other parameter, that sets the normalization of $n(r)$, cancels out in the Jeans equation. We find $r_n = 0.27^{+0.44}_{-0.15}$ Mpc, and a background density corresponding to 38% background contamination in our $z_{\rm p}$-selected sample.

Since the uncertainties on r_n are very large, we also consider an alternative estimate, based on the spectroscopic sample of cluster members (see Sect. 5.1). The radial geometrical completeness, $C_g(R)$, is the same for this sample as for the $z_{\rm p}$-selected sample. In addition, the spectroscopic sample suffers from radially-dependent completeness because the fraction of galaxies with measured redshifts is higher near the cluster center. We evaluate this spectroscopic completeness, $C_s(R)$, as the ratio of the number of galaxies with measured redshifts to the total number of galaxies (134 and 713 in total) in radial bins, down to $F814 \leq 23$. We find $C_s(R) = 0.22$ outside the central bin, i.e. at $R \geq 0.11$ arcmin, and $C_s(R) = 0.50$ inside this bin. We then run a maximum-likelihood fit of the spatial distribution of spectroscopic members weighting each galaxy by $[C_g(R_i) \times C_s(R_i)]^{-1}$. We find $r_n = 0.48^{+0.46}_{-0.24}$ Mpc, and a background density corresponding to 4% background contamination. The background contamination, which is much lower than for the $z_{\rm p}$-selected sample, as expected. The r_n value is consistent within the (large) error bars with that obtained using the z_p-selected sample.

In the dynamical analysis with the DK and MAMPOSSt methods, we will use both estimates of r_n, to understand how much our limited knowledge of r_n affects our estimate of the cluster mass profile. The knowledge of r_n is not required for the dynamical analysis with the Caustic method.

5.3. Results

For both the DK and MAMPOSSt methods we use the NFW model for $M(r)$ (Navarro et al. 1997),

$$M(r) = M_{200} \frac{\ln(1 + r/r_{-2}) - r/r_{-2}\,(1 + r/r_{-2})^{-1}}{\ln(1 + c_{200}) - c_{200}/(1 + c_{200})}, \quad (10)$$

where $c_{200} \equiv r_{200}/r_{-2}$ is the mass profile concentration. The model has two free parameters, the virial mass and concentration, or, equivalently, the virial and scale radii r_{200} and r_{-2}. Note that the total mass density scale-length is different from the scale-radius of the galaxy number density profile, i.e. $r_{-2} \neq r_n$ (Sect. 5.2), since we allow the ditribution of the total mass and that of the galaxies to be different in our analysis. For the Caustic technique, for the sake of comparison with the other two methods, we also fit a NFW model to the mass density profile determined from differentiation of the non-parametrically determined mass profile.

The MAMPOSSt method is the only one among the three where there is complete freedom in the choice of $\beta(r)$. We use a simplified version of the model of Tiret et al. (2007), $\beta(r) = \beta_\infty\, r/(r + r_{-2})$, where β_∞ is the asymptotic value of the anisotropy reached at large radii, and r_{-2} is the scale radius of the NFW mass density distribution. This model was shown by Mamon et al. (2010) to provide a good fit to cluster-mass halos extracted from cosmological numerical simulations. In this model, galaxy orbits are isotropic near the cluster center and become increasingly radially anisotropic outside.

In the Caustic technique, we use Gaussian adaptive kernels for the density estimation in projected phase space, with an initial kernel size equal to the optimal kernel size of Silverman (1986). Before the density estimation, we scale the velocity coordinates such that the scaled velocity dispersion is the same as the dispersion in the radial coordinates. In the equation that connects $M(r)$ to the Caustic amplitude (eq. 13 in Diaferio 1999), we adopt either $\mathcal{F}_\beta = 0.5$ as recommended by Diaferio (1999) and Geller et al. (2013), or $\mathcal{F}_\beta = 0.7$ as recommended by Serra et al. (2011). For the estimation of the $M(r)$ error we adopt the recipe of Diaferio (1999). Serra et al. (2011) have found that these error estimates correspond to 50% confidence levels; we therefore scale them up by a factor of 1.4 to have $\sim 1\sigma$ level error estimates. The chosen caustic is displayed in Fig. 6.

The domain of application of the DK and MAMPOSSt methods is the virial region. Since almost all our cluster members are in the virial region, we only exclude the very central region, 25 kpc, where the gravitational potential is likely to be dominated by the cD and therefore unlikely to follow a purely NFW profile.

The results of the dynamical analysis are summarized in Table 5 and displayed in Fig. 10, where we show the confidence contour in the $[r_{200}, r_{-2}]$ plane. We also list and display a weighted average of the DK, MAMPOSSt, and Caustic results. We multiply the formal error on this average by $\sqrt{5}$ to take into account that the five averaged results are not independent. The constraints on the β parameters obtained by the DK and MAMPOSSt methods are very loose, so we do not display them here.

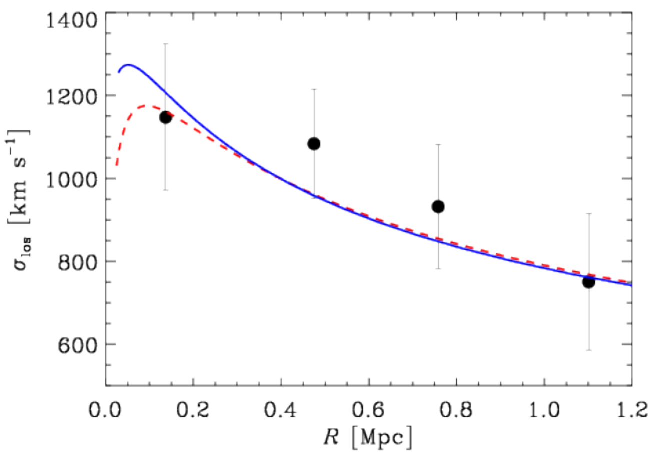

Fig. 9. The observed line of sight velocity dispersion profile (points with 1 σ error bars) and those predicted by the best-fit NFW models, obtained with the DK (dashed red line), and MAMPOSSt (solid blue line) methods. Only those solutions obtained using the r_n value found with the z_p sample of members are shown, for clarity.

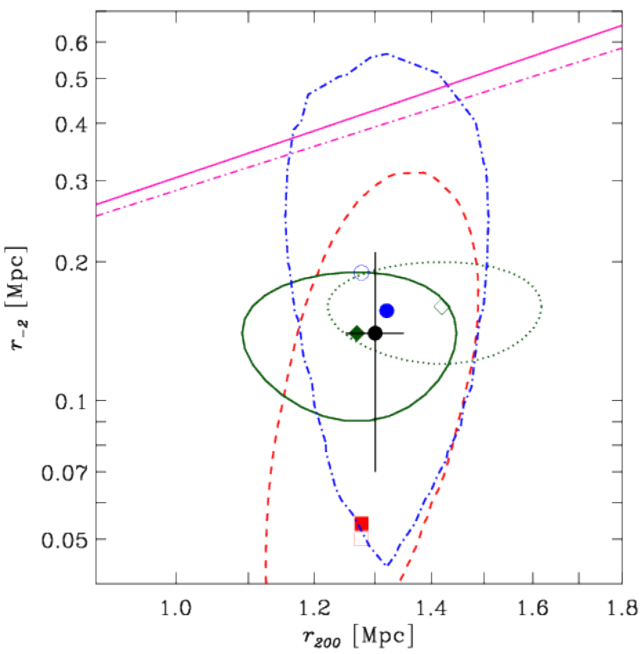

Fig. 10. The best-fit $M(r)$ NFW parameters from the kinematics analyses, within 1 σ confidence level contours, obtained with the DK (red squares), MAMPOSSt (blue dot and circle), and Caustic (green filled and open diamond) methods. The filled (resp. open) symbols are for the solutions obtained using the r_n value from the photometric (resp. spectroscopic) sample of members. The dashed red (resp. dash-dotted blue) contour represents the 1 σ confidence region on the best-fit parameters of the DK (resp. MAMPOSSt) method, obtained using the r_n value from the photometric sample of members. The solid (resp. dotted) green contour represents the 1 σ confidence region on the best-fit parameters for the Caustic method obtained using $\mathcal{F}_\beta = 0.5$ (resp. $\mathcal{F}_\beta = 0.7$). The magenta solid (resp. dash-dotted) inclined line is the theoretical predictions for relaxed clusters at the mean redshift of LCDCS 0504 from Bhattacharya et al. (2013) (resp. De Boni et al. 2013). The black dot with error bars is the weighted average of the DK, MAMPOSSt and Caustic results.

Table 5. Best-fit $M(r)$ and β parameters from kinematics.

Method	r_{200} [Mpc]	r_{-2} [Mpc]	Velocity anisotropy
DK (p)	$1.28^{+0.16}_{-0.06}$	$0.05^{+0.26}_{-0.03}$	-3^{+3}_{-1}
DK (s)	$1.28^{+0.12}_{-0.10}$	$0.05^{+0.35}_{-0.05}$	-3^{+3}_{-2}
MAMPOSSt (p)	$1.32^{+0.14}_{-0.09}$	$0.16^{+0.34}_{-0.10}$	$0.5^{+0.4}_{-0.2}$
MAMPOSSt (s)	$1.28^{+0.10}_{-0.12}$	$0.19^{+0.43}_{-0.12}$	$0.5^{+0.4}_{-0.2}$
Caustic, $\mathcal{F}_\beta = 0.5$	$1.27^{+0.16}_{-0.20}$	$0.14^{+0.06}_{-0.04}$	–
Caustic, $\mathcal{F}_\beta = 0.7$	$1.42^{+0.18}_{-0.22}$	$0.16^{+0.04}_{-0.04}$	–
Weighted average	1.30 ± 0.05	0.14 ± 0.07	–

Notes. The DK and MAMPOSSt estimates are obtained using the number density profile based on the photometric (p) or the spectroscopic (s) samples of cluster members. The velocity anisotropy is the constant value of β for the DK method, and β_∞ in the simplified Tiret model for the MAMPOSSt method.

There is a good agreement between the values of r_{200} obtained by the DK, MAMPOSSt and Caustic methods. The Caustic solution obtained with $\mathcal{F}_\beta = 0.5$ is closer to those from the other two methods. This would argue in favor of using this value, rather than $\mathcal{F}_\beta = 0.7$, in the Caustic technique, as done recently by Geller et al. (2013). However, Gifford et al. (2013) have recently suggested using the intermediate value $\mathcal{F}_\beta$=0.65. Moreover, for β = cst NFW models, at the half-mass radius of $\approx 2\,r_{-2}$, $\mathcal{F}_\beta = 0.5$ corresponds to $\beta = -1.1$ while $\mathcal{F}_\beta = 0.7$ corresponds to $\beta = 0.3$. The very tangential anisotropy for $\mathcal{F}_\beta = 0.5$ is not what most analysis extract for galaxies in clusters (e.g. Biviano et al. 2013, and references therein), so the agreement of the $\mathcal{F}_\beta = 0.5$ solution with those of the DK and MAMPOSSt methods may just be fortuitous.

The DK and MAMPOSSt methods pose very weak constraints on r_{-2}. Mamon et al. (2013) already noted that the determination of the dark matter scale radius is inefficient, which Sanchis et al. (2004) had previously noted for the concentration parameter. The constraints obtained by the Caustic technique are tighter, and almost independent of the value of $\mathcal{F}_\beta$. The Caustic technique is able to better constrain the r_{-2} parameter of the mass distribution than the DK and MAMPOSSt techniques possibly because, unlike these, it is the only free parameter in the model fit. In fact $\beta(r)$ is fixed when the value of $\mathcal{F}_\beta$ is assumed, and r_{200} is estimated non-parametrically directly from the Caustic mass profile.

The agreement between the MAMPOSSt and DK solutions is also evident from Fig. 9 where we show the projection of the best-fit DK and MAMPOSSt solutions on the observed line-of-sight velocity dispersion profile[8].

In Fig. 10 we also show the theoretical predictions of Bhattacharya et al. (2013) and De Boni et al. (2013) for the concentration-mass relation of relaxed clusters at the redshift of LCDCS 0504, converted in the r_{200}-r_{-2} plane. Both theoretical predictions predict too high a concentration for a cluster of the mass and at the redshift of LCDCS 0504. Since the prediction of De Boni et al. (2013) is based on hydrodynamic simulations, while that of Bhattacharya et al. (2013) originates from DM-only simulations, the discrepancy between theoretical predictions and observation cannot be explained by baryonic processes affecting the cluster dynamical structure.

6. Comparing the different mass profile determinations

The methods based on SL, X-ray, and kinematics to determine the cluster mass profile have different sensitivities on different scales. It would therefore be misleading to either extrapolate the SL and X-ray mass estimates to r_{200} to compare with the result from kinematics, or to restrict the spectroscopic data-sample to a smaller region to directly infer r_{2500} or r_{500} from the kinematics analysis, with loss of statistics. Rather than comparing the mass profile parameters, a more appropriate comparison is that between the different mass profiles themselves, in the regions where they overlap.

The three $M(r)$ from the SL, X-ray, and kinematics analyses are shown in the top panel of Fig. 11, their ratios are shown in the bottom panel of the same figure[9]. The SL and kinematics $M(r)$ are in agreement within the errors. The significant difference in the r_{200} values of these two profiles is therefore due to the uncertain extrapolation of the SL $M(r)$, which is considerably flatter than the kinematics $M(r)$. On the other hand, within inner 100 kpc, the $M(r)$ obtained by the X-ray analysis is significantly below both the SL and the kinematics mass profiles. In this case, the discrepancy is real and cannot be attributed to extrapolation uncertainties.

We will discuss the possible origin of the differences between the mass profiles in Sect. 8.

7. The gas mass fraction

We compute the intra-cluster gas mass profile with the integral of the gas density profile of equation (6) over a spherical volume. For the present cluster we have:

$$M_{\rm gas}(r) = 1.205 \times 10^8\, n_0\, r^3\, {}_2F_1\left(\frac{3}{2}, \frac{3\beta_X}{2}, \frac{5}{2}, -\frac{r^2}{r_c^2}\right) M_\odot\,, \qquad (11)$$

where ${}_2F_1(a, b, c, x)$ is the standard hypergeometric function.[10]

Dividing Eq. (11) by Eq. (7) yields the gas mass fraction, $f_{\rm gas}$. Figure 12 shows the mass profiles, gas and total, in the upper panel and the gas fraction radial profile in the bottom panel. The cluster gas mass fraction increases with r, as seen in most

[8] We remind the reader that the DK best-fit solution is obtained by a simultaneous fit of both the observed velocity dispersion profile and the observed kurtosis profile, while the MAMPOSSt best-fit solution is obtained by a fit of the full line-of-sight velocity distribution. Fig. 9 is just a way of presenting the best-fit models.

[9] To compare the mass distribution obtained with the SL analyses with the others, we take the spherical approximation also for the SL method. In practice we force to zero the ellipticity parameter ϵ of the SL model.

[10] For $\beta_X = 1/2$, consistent with our fit to the X-ray surface brightness profile, a useful approximation to the hypergeometric function of equation (11) is ${}_2F_1\left(\frac{3}{2}, \frac{3}{4}, \frac{5}{2}, -\frac{r^2}{r_c^2}\right) \simeq 6\left[(x^3/3)^{-\gamma} + (2x^3/3)^{-\gamma}\right]^{-1/\gamma}$, where $\gamma = 2^{1/8} \simeq 1.0905$, which is accurate to better than 2.7% for all radii (see Mamon & Łokas 2005).

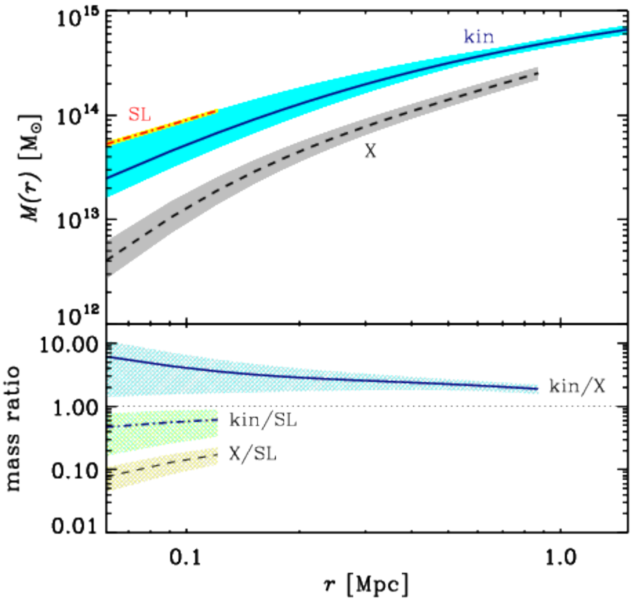

Fig. 11. *Top panel:* The mass profiles and their 1 σ confidence regions obtained from the SL (red dashed line and yellow region), X-ray (black dashed line and grey region), and kinematics (blue solid line and cyan region) analyses. *Bottom panel:* the ratios of the three mass profiles and their 1 σ confidence regions. Solid blue line and grey-cyan region: ratio of the kinematics to X-ray mass profiles. Dashed-dotted blue line and green region: ratio of the kinematics to SL mass profiles. Dashed black line and orange region: ratio of the X-ray to SL mass profiles. In both panels the profiles are shown in the radial range where they are constrained by the data.

clusters (see, e.g., Biviano & Salucci 2006; Allen et al. 2008; Frederiksen et al. 2009). At $r > 300$ kpc, the gas mass fraction reaches a value that is consistent with the cosmic gas fraction, which is $\simeq 83\%$ of the cosmic baryon fraction (Fukugita et al. 1998; Hinshaw et al. 2012; Planck Collaboration et al. 2013a).

A comparison with the results of Eckert et al. (2013) shows that the gas mass fraction profile of LCDCS 0504 is very similar to that of lower-z clusters, except near the cluster center, where it is significantly below. This is shown in the top panel of Fig. 13 where we plot the results of Eckert et al. (2013) for the average gas mass fraction of cool-core and non-cool-core clusters, together with our results, based in both cases on the total mass determined from X-ray analysis. If we instead use the total mass determined from kinematics, we can compare our result with that of Biviano & Salucci (2006). This comparison is shown in the bottom panel of Fig. 13. In this case the gas fraction of LCDCS 0504 appears to lie below that for a sample of nearby clusters at almost all radii.

Finally, we compare the LCDCS 0504 gas mass fraction computed using the total mass derived from our lensing analysis (see Sect. 3) with those of Zhang et al. (2010), also derived using total mass estimates from lensing, except that in their case it was the weak, not the strong lensing effect that was used. The comparison is shown in Fig. 14, where we plot the gas mass fractions as a function of the cluster mass, both determined at r_{2500}. This is the smallest radius at which Zhang et al. (2010) have given their determinations and still it is beyond the region where SL is detected in LCDCS 0504, $r_{2500} = 0.49$ Mpc for the SL $M(r)$. From Fig. 14 we see that the gas mass fraction of LCDCS 0504 at this radius is not anomalous. This is consistent with the conclusions we obtained using the X-ray- and kinematics-determined total masses (Fig. 13), LCDCS 0504 shows an anomalous (low) gas mass fraction only at small radii.

We will discuss in the next Section the possible origin of this central gas fraction deficiency.

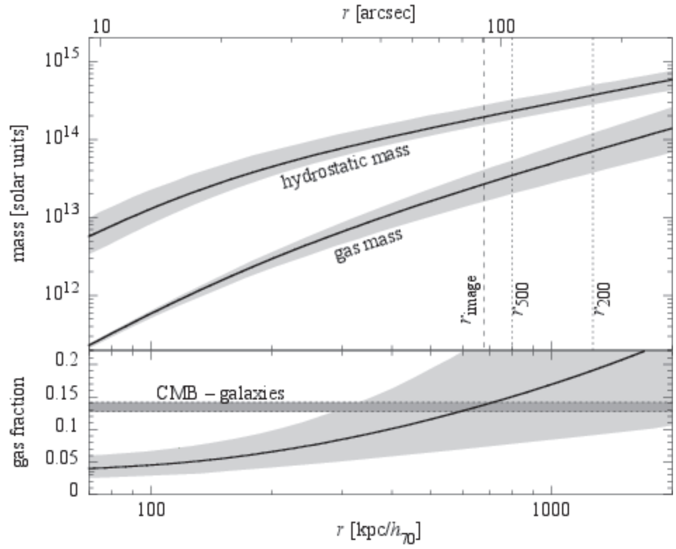

Fig. 12. *Top panel*: The intra-cluster gas mass profile (lower curve) and the hydrodynamical derived total mass radial profiles. The grey shaded regions represent 1σ confidence levels. Vertical lines indicate r_{image}, the limit where the cluster is detected with the combined XMM data (using both exposures), and r_{500} and r_{200}, computed from the X-ray derived mass profile. *Bottom panel*: the gas mass fraction radial profile. As a reference we also show the universal gas fraction, as obtained by the cosmic baryon fraction Ω_b/Ω_m value from WMAP-9yr (Hinshaw et al. 2012) and Planck 1st release (Planck Collaboration et al. 2013a) (including their uncertainties), reduced by 17%

8. Discussion and conclusions

We have analyzed the mass profile $M(r)$ of a $z \approx 0.8$ cluster with the SL technique, using the X-ray emission from the intra-cluster hot gas, and using galaxies as tracers of the gravitational potential. The different determinations of the cluster $M(r)$ disagree, especially in the inner regions. The SL $M(r)$ is slightly above but still consistent with the kinematic determination, but both are significantly above the X-ray $M(r)$ determination.

This discrepancy is unlikely to be caused by an unrelaxed dynamical status of the cluster. This could cause an overestimate of the cluster velocity dispersion and hence the cluster mass estimate from kinematics (see, e.g., Biviano et al. 2006) and an incomplete thermalization of the intra-cluster gas, leading to an underestimate of the cluster mass estimates from X-ray (e.g. Rasia et al. 2006), but it would not affect the lensing mass estimate. Moreover, an unrelaxed dynamical status is not supported by the analyses of substructures by Guennou et al. (2013). In that paper, we have used the Serna & Gerbal (1996, SG hereafter) hierarchical method for the detection of substructures in the distribution of galaxies and searched for substructures in the X-ray data (described in Sect. 2.1), by analysing the residuals of the subtraction of a symmetric elliptical β-model from the X-ray image (see Guennou et al. 2013 for details). Seven substructures were detected by the SG technique, all with masses below 10%

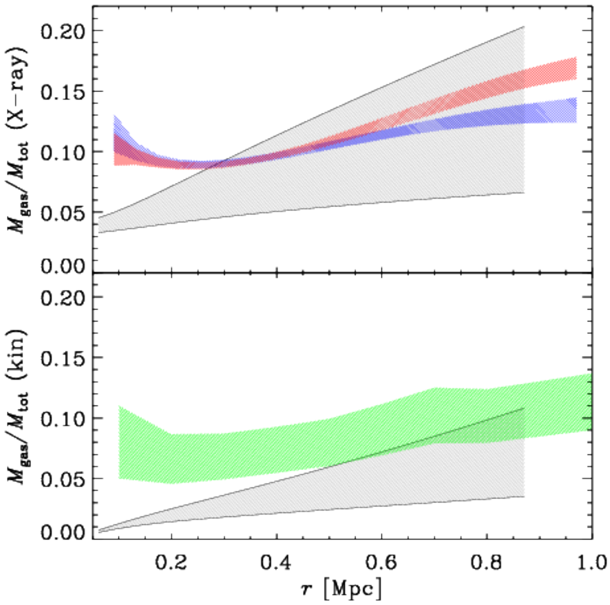

Fig. 13. *Top panel:* The ratio of gas mass to total mass from the X-ray analysis. The grey shaded region within solid lines is the 1 σ interval on the observed gas mass fraction of LCDCS 0504. The blue and red shaded regions (the blue one below the red one at large radii) are the average gas mass fractions for cool-core and non-cool-core clusters from Eckert et al. (2013). *Bottom panel:* The ratio of gas mass to total mass, the latter derived from the kinematics analysis. The grey shaded region within solid lines is the 1 σ interval on the observed gas mass fraction of LCDCS 0504. The green shaded region is the average gas mass fraction for nearby clusters from Biviano & Salucci (2006).

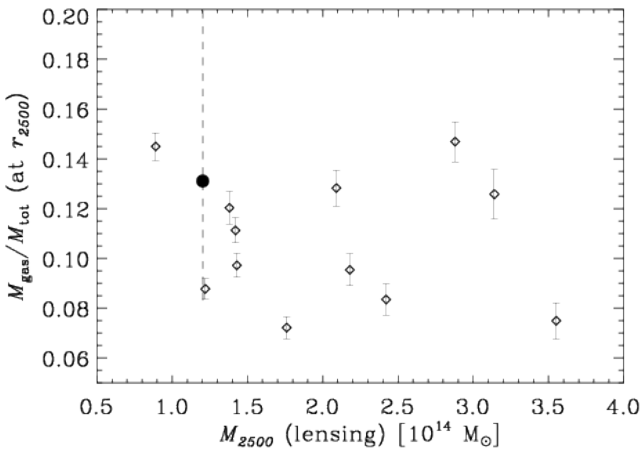

Fig. 14. The ratio of gas mass to total mass determined from lensing analyses for the clusters of Zhang et al. (2010) (diamonds) and for LCDCS 0504 (dot). Error bars are 1 σ.

of the total cluster mass. Of these, only one was also detected in X-rays, with an X-ray luminosity of $\approx 8\%$ the total cluster X-ray luminosity. This analysis indicates that any major perturbation of the LCDCS 0504 dynamical status must thus have occurred sufficiently long ago for the remnants of the merging groups to have disappeared.

Another interesting possibility is that we see the cluster with its major axis along the line-of-sight. This is suggested by the circularly symmetric SL configuration and by the small ellipticity of the cD galaxy, since the elongation of cD galaxies generally reflects those of their host clusters (e.g. Rhee & Katgert 1987; Kim et al. 2002) (see Fig. 1). It has been shown both on numerical simulations (Kasun & Evrard 2005) and observationally (Wojtak 2013), that clusters are prolate not only in position space but also in velocity space, and the major axes of the spatial and velocity distributions are aligned. The orientation of the cluster with the major axis along the line-of-sight then results in an overestimate of the cluster mass estimatd from SL and velocity dispersion. According to Wojtak (2013), the mean ratio of the velocity dispersions along the minor and major axes of a cluster is $\simeq 0.78$. This implies a ratio of the velocity dispersion along the major axis to the mean cluster velocity dispersion of 1.16, i.e. a 32% mass overestimate at a given radius. This is still not sufficient to remove the systematic difference between the mass profile derived from kinematics and that derived by the X-ray analysis.

The alignment effect just discussed could also induce an overestimate of mass profile concentration value. This could explain the disagreement we find with the theoretical predictions of Bhattacharya et al. (2013) and De Boni et al. (2013) (see Fig. 10).

Whatever the cause for the X-ray vs. kinematics and SL $M(r)$ discrepancy, substantial systematic underestimates of cluster masses by the X-ray methodology could be interesting for cosmology, as it could alleviate the tension between the σ_8 values found by the Planck collaboration using the Cosmic Microwave Background power-spectrum on one hand and cluster counts obtained by the Sunyaev-Zeldovich effect (using X-ray masses as mass calibrators Planck Collaboration et al. 2013b): If X-ray masses are underestimated at given SZ signal, this means the distribution of SZ counts above a given mass threshold is underestimated, meaning that Ω_m (σ_8) is underestimated (overestimated), which would bring the best-fit value more in line with the CMB value.

Another intriguing result of our analysis is the discovery that the gas mass fraction is anomalously low near the center of the LCDCS 0504 cluster. Given the relaxed, symmetric morphology of the X-ray emission (see Fig. 3), it is unlikely that this anomaly could be attributed to the effects of a major merger displacing the gas from the center, as in the case of the Bullet cluster (Barrena et al. 2002; Markevitch et al. 2002). Alternatively, the gas could have been ejected by AGN outbursts, while the effects of SNe explosions should not be significant (Conroy & Ostriker 2008; Dubois et al. 2013). Dubois et al. (2013) predict a 30% loss in the core due to AGN outflows, which is not to far from our observed deficiency (with respect to the average of other clusters) of $\simeq 60\%$ (see Fig. 13), given the large observational uncertainties.

The main issue with the AGN hypothesis is that there is no evidence of a radio source in the NVSS catalog or in the X-rays as there is no detectable point source at the location of the cD, although there is a hint of a cool core. Also, we have no evidence of broad lines in the optical spectrum of the cD. All this lack of evidence does, however, tell us, is that the assumed AGN activity have subsided long enough ago so that all strong electromagnetic signatures of AGN activity have now subsided.

In the near future, we plan to extend the dynamical and structural analysis presented here to clusters with sufficient spectroscopic information in the full DAFT/FADA cluster set. Expanding our data-sets should allow us to determine if the anomalies identified in LCDCS 0504 are a characteristic of high-z clusters or not. Hopefully, with a larger sample we will be able to unveil the hidden systematics causing discrepant determinations of cluster mass profiles by different methods, and to relate these systematics to the currently not well understood physics of the intra-cluster baryons.

Acknowledgements. We wish to express our sincere condolences and grief to the family of Alain Mazure who unexpectedly passed away during the preparation of this paper. We wish to thank the anonymous referee for her/his suggestions. ML acknowledges the Centre National de la Recherche Scientifique (CNRS) for its support. The Dark Cosmology Centre is funded by the Danish National Research Foundation. This work has been conducted using facilities offered by CeSAM (Centre de donnéeS Astrophysique de Marseille – http://www.lam.fr/cesam/). FD acknowledges long-term support from CNES and CAPES/COFECUB program 711/11. AB acknowledges the hospitality of the Inst. d'Astroph. de Paris and of the Obs. de la Côte d'Azur. This research has made use of the NASA/IPAC Extragalactic Database (NED) which is operated by the Jet Propulsion Laboratory, California Institute of Technology, under contract with the National Aeronautics and Space Administration. GBLN and ESC acknowledge the support of the Brazilian funding agencies FAPESP and CNPq. Based on observations obtained at the Gemini Observatory, which is operated by the Association of Universities for Research in Astronomy, Inc., under a cooperative agreement with the NSF on behalf of the Gemini partnership: the National Science Foundation (United States), the National Research Council (Canada), CONICYT (Chile), the Australian Research Council (Australia), Ministério da Ciência, Tecnologia e Inovação (Brazil) and Ministerio de Ciencia, Tecnología e Innovación Productiva (Argentina). I.M. acknowledges financial support from the Spanish grant AYA2010-15169 and from the Junta de Andalucia through TIC-114 and the Excellence Project P08-TIC-03531.

References

Adami, C., Biviano, A., Durret, F., & Mazure, A. 2005, A&A, 443, 17
Allen, S. W., Rapetti, D. A., Schmidt, R. W., et al. 2008, MNRAS, 383, 879
Anders, E. & Grevesse, N. 1989, Geochim. Cosmochim. Acta, 53, 197
Balucinska-Church, M. & McCammon, D. 1992, ApJ, 400, 699
Bardeau, S., Kneib, J., Czoske, O., et al. 2005, A&A, 434, 433
Barrena, R., Biviano, A., Ramella, M., Falco, E. E., & Seitz, S. 2002, A&A, 386, 816
Bartelmann, M. 1996, A&A, 313, 697
Beers, T. C., Flynn, K., & Gebhardt, K. 1990, AJ, 100, 32
Bhattacharya, S., Habib, S., Heitmann, K., & Vikhlinin, A. 2013, ApJ, 766, 32
Binney, J. & Tremaine, S. 1987, Galactic dynamics (Princeton, NJ, Princeton University Press, 1987, 747 p.)
Biviano, A. 2006, in EAS Publications Series, ed. G. A. Mamon, F. Combes, C. Deffayet, & B. Fort, 171–178
Biviano, A., Durret, F., Gerbal, D., et al. 1996, A&A, 311, 95
Biviano, A. & Girardi, M. 2003, ApJ, 585, 205
Biviano, A. & Katgert, P. 2004, A&A, 424, 779
Biviano, A., Murante, G., Borgani, S., et al. 2006, A&A, 456, 23
Biviano, A., Rosati, P., Balestra, I., et al. 2013, A&A, 558, A1
Biviano, A. & Salucci, P. 2006, A&A, 452, 75
Böhringer, H., Pratt, G. W., Arnaud, M., et al. 2010, A&A, 514, A32
Borgani, S. & Guzzo, L. 2001, Nature, 409, 39
Briel, U. G., Henry, J. P., Schwarz, R. A., et al. 1991, A&A, 246, L10
Cavaliere, A. & Fusco-Femiano, R. 1976, A&A, 49, 137
Coe, D., Benítez, N., Broadhurst, T., & Moustakas, L. A. 2010, ApJ, 723, 1678
Conroy, C. & Ostriker, J. P. 2008, ApJ, 681, 151
Cypriano, E. S., Sodré, Jr., L., Kneib, J.-P., & Campusano, L. E. 2004, ApJ, 613, 95
De Boni, C., Ettori, S., Dolag, K., & Moscardini, L. 2013, MNRAS, 428, 2921
DeCarlo, L. T. 1997, Psychological Methods, 2, 292
den Hartog, R. & Katgert, P. 1996, MNRAS, 279, 349
Diaferio, A. 1999, MNRAS, 309, 610
Diaferio, A. & Geller, M. J. 1997, ApJ, 481, 633
Dressler, A. & Shectman, S. A. 1988, AJ, 95, 985
Dubois, Y., Pichon, C., Devriendt, J., et al. 2013, MNRAS, 428, 2885
Eckert, D., Ettori, S., Molendi, S., Vazza, F., & Paltani, S. 2013, A&A, 551, A23
Elíasdóttir, Á., Limousin, M., Richard, J., et al. 2007, arXiv:astro-ph/0710.5636, Vol. 710
Escalera, E., Biviano, A., Girardi, M., et al. 1994, ApJ, 423, 539
Frederiksen, T. F., Hansen, S. H., Host, O., & Roncadelli, M. 2009, ApJ, 700, 1603
Fukugita, M., Hogan, C. J., & Peebles, P. J. E. 1998, ApJ, 503, 518
Geller, M. J., Diaferio, A., Rines, K. J., & Serra, A. L. 2013, ApJ, 764, 58
Gifford, D., Miller, C., & Kern, N. 2013, ApJ, 773, 116
Girardi, M. & Biviano, A. 2002, Optical Analysis of Cluster Mergers (ASSL Vol. 272: Merging Processes in Galaxy Clusters), 39–77
Guennou, L., Adami, C., Durret, F., et al. 2013, arXiv:1311.6922
Guennou, L., Adami, C., Ulmer, M. P., et al. 2010, A&A, 523, A21
Halliday, C., Milvang-Jensen, B., Poirier, S., et al. 2004, A&A, 427, 397
Hinshaw, G., Larson, D., Komatsu, E., et al. 2012, arXiv:1212.5226
Jee, M. J., White, R. L., Benítez, N., et al. 2005, ApJ, 618, 46
Johnson, O., Best, P., Zaritsky, D., et al. 2006, MNRAS, 371, 1777
Jullo, E., Kneib, J.-P., Limousin, M., et al. 2007, New Journal of Physics, 9, 447
Kaastra, J. S. & Mewe, R. 1993, A&AS, 97, 443
Kalberla, P. M. W., Burton, W. B., Hartmann, D., et al. 2005, A&A, 440, 775
Kasun, S. F. & Evrard, A. E. 2005, ApJ, 629, 781
Katgert, P., Biviano, A., & Mazure, A. 2004, ApJ, 600, 657
Kent, S. M. & Gunn, J. E. 1982, AJ, 87, 945
Kim, R. S. J., Annis, J., Strauss, M. A., & Lupton, R. H. 2002, in Astronomical Society of the Pacific Conference Series, Vol. 268, Tracing Cosmic Evolution with Galaxy Clusters, ed. S. Borgani, M. Mezzetti, & R. Valdarnini, 395
Leonard, A., King, L. J., & Goldberg, D. M. 2011, MNRAS, 413, 789
Liedahl, D. A., Osterheld, A. L., & Goldstein, W. H. 1995, ApJ, 438, L115
Limousin, M., Kneib, J. P., Bardeau, S., et al. 2007a, A&A, 461, 881
Limousin, M., Kneib, J.-P., & Natarajan, P. 2005, MNRAS, 356, 309
Limousin, M., Richard, J., Jullo, E., et al. 2007b, ApJ, 668, 643
Łokas, E. L. & Mamon, G. A. 2001, MNRAS, 321, 155
Łokas, E. L. & Mamon, G. A. 2003, MNRAS, 343, 401
Łokas, E. L., Wojtak, R., Gottlöber, S., Mamon, G. A., & Prada, F. 2006, MNRAS, 367, 1463
Mamon, G. A., Biviano, A., & Boué, G. 2013, MNRAS, 429, 3079
Mamon, G. A., Biviano, A., & Murante, G. 2010, A&A, 520, A30
Mamon, G. A. & Łokas, E. L. 2005, MNRAS, 363, 705
Markevitch, M., Gonzalez, A. H., Clowe, D., et al. 2004, ApJ, 606, 819
Markevitch, M., Gonzalez, A. H., David, L., et al. 2002, ApJ, 567, L27
Mohr, J. J., Fabricant, D. G., & Geller, M. J. 1993, ApJ, 413, 492
Navarro, J. F., Frenk, C. S., & White, S. D. M. 1997, ApJ, 490, 493
Nelson, A. E., Gonzalez, A. H., Zaritsky, D., & Dalcanton, J. J. 2001, ApJ, 563, 629
Neumann, D. M., Arnaud, M., Gastaud, R., et al. 2001, A&A, 365, L74
O'Hara, T. B., Mohr, J. J., & Guerrero, M. A. 2004, ApJ, 604, 604
Planck Collaboration, Ade, P. A. R., Aghanim, N., et al. 2013a, arXiv:1303.5076
Planck Collaboration, Ade, P. A. R., Aghanim, N., et al. 2013b, arXiv:1303.5080
Pratt, G. W., Böhringer, H., & Finoguenov, A. 2005, A&A, 433, 777
Ramella, M., Biviano, A., Pisani, A., et al. 2007, A&A, 470, 39
Rasia, E., Ettori, S., Moscardini, L., et al. 2006, MNRAS, 369, 2013
Rhee, G. F. R. N. & Katgert, P. 1987, A&A, 183, 217
Sanchis, T., Łokas, E. L., & Mamon, G. A. 2004, MNRAS, 347, 1198
Serna, A. & Gerbal, D. 1996, A&A, 309, 65
Serra, A. L., Diaferio, A., Murante, G., & Borgani, S. 2011, MNRAS, 412, 800
Silverman, B. W. 1986, Density estimation for statistics and data analysis
Tiret, O., Combes, F., Angus, G. W., Famaey, B., & Zhao, H. S. 2007, A&A, 476, L1
van der Marel, R. P., Magorrian, J., Carlberg, R. G., Yee, H. K. C., & Ellingson, E. 2000, AJ, 119, 2038
Wojtak, R. 2013, arXiv:1310.3624
Wojtak, R. & Łokas, E. L. 2010, MNRAS, 408, 2442
Wojtak, R., Łokas, E. L., Mamon, G. A., & Gottlöber, S. 2009, MNRAS, 399, 812
Wojtak, R., Łokas, E. L., Mamon, G. A., et al. 2007, A&A, 466, 437
Zhang, Y.-Y., Okabe, N., Finoguenov, A., et al. 2010, ApJ, 711, 1033

Table 2. Coordinates, magnitudes, and redshifts of the LCDCS 0504 spectroscopic galaxy catalogue. Asterisks mark data from our GMOS run.

RA (J2000)	Dec (J2000)	*I*	redshift	RA (J2000)	Dec (J2000)	*I*	redshift
12 16 35.84	−12 03 16.4	22.20	0.7850	12 16 44.70	−12 01 28.2	21.28	0.7865
12 16 35.90	−12 00 29.4	21.62	0.7930	12 16 44.72	−12 01 23.4	22.25	0.7945
12 16 36.13	−12 00 43.8	22.04	0.6740*	12 16 44.74	−11 59 16.2	22.10	0.7998
12 16 36.14	−11 59 01.4	21.52	0.4816	12 16 44.84	−12 01 30.9	21.97	0.7984
12 16 36.27	−12 03 29.0	21.34	0.5894	12 16 44.87	−12 01 20.3	21.54	0.8035
12 16 36.37	−11 59 20.0	22.74	0.6650*	12 16 44.87	−12 00 43.5	22.93	0.7824
12 16 36.41	−12 00 08.7	21.64	0.7868	12 16 44.91	−12 02 13.9	20.90	0.6691
12 16 36.51	−12 00 31.9	22.38	0.6740*	12 16 44.91	−12 02 03.6	21.50	0.7938
12 16 36.54	−12 02 29.8	22.90	0.4700*	12 16 45.09	−11 58 49.3	21.18	0.7969
12 16 36.62	−12 02 29.8	22.00	0.4700*	12 16 45.12	−12 00 35.9	23.02	0.7883
12 16 37.18	−12 00 41.9	21.03	0.6606	12 16 45.18	−11 58 20.0	21.54	0.2327
12 16 37.74	−12 03 48.6	21.72	0.7940	12 16 45.24	−12 03 13.4	21.60	0.7933
12 16 38.01	−12 02 51.4	21.89	0.7900*	12 16 45.26	−12 01 17.6	20.66	0.7955
12 16 38.12	−12 03 26.6	21.26	0.7939	12 16 45.32	−12 01 20.9	21.30	0.8054
12 16 38.23	−12 02 51.7	21.08	0.7900	12 16 45.37	−12 00 01.7	21.70	0.7996
12 16 38.40	−11 59 15.2	20.62	0.2758	12 16 45.60	−11 58 38.3	22.85	0.7925
12 16 38.74	−12 01 50.3	21.50	0.8008	12 16 45.65	−12 01 08.0	21.64	0.8058
12 16 38.74	−12 03 12.0	21.19	0.7958	12 16 45.83	−12 01 05.6	22.94	0.7921
12 16 38.83	−12 02 44.2	20.79	0.4167	12 16 45.91	−12 03 29.4	21.69	0.2252
12 16 39.08	−12 00 15.6	22.40	0.8890*	12 16 46.10	−12 01 14.3	20.61	0.7997
12 16 39.08	−12 03 35.7	22.55	0.6601	12 16 46.18	−12 02 25.3	21.55	0.7866
12 16 39.11	−11 58 53.6	21.59	0.6640*	12 16 46.20	−12 00 31.0	22.27	0.7952
12 16 39.13	−11 58 39.9	21.60	0.6650*	12 16 46.23	−12 00 07.3	22.06	0.7847
12 16 39.24	−11 58 03.4	22.41	0.8816	12 16 46.35	−12 03 25.7	22.34	0.7966
12 16 39.41	−12 03 46.4	21.05	0.5888	12 16 46.39	−11 59 34.0	22.64	0.7936
12 16 39.69	−12 03 07.2	22.00	0.5437	12 16 46.67	−11 59 37.8	21.77	0.6669
12 16 39.88	−11 58 17.0	20.55	0.2727	12 16 46.83	−12 02 22.6	21.39	0.7987
12 16 39.91	−11 59 52.9	22.81	0.7416	12 16 46.90	−12 01 23.9	22.40	0.7910*
12 16 39.96	−11 58 48.1	20.50	0.2329	12 16 46.97	−11 59 26.7	21.70	0.7971
12 16 40.05	−12 02 35.2	21.12	0.8022	12 16 47.61	−12 02 28.0	20.41	0.5434
12 16 40.19	−12 01 59.3	19.34	0.3463	12 16 48.00	−12 00 22.0	21.74	0.7860
12 16 40.27	−12 02 02.9	22.18	0.7976	12 16 48.18	−12 03 18.6	22.73	0.8039
12 16 40.27	−11 58 19.8	22.90	0.6655	12 16 48.42	−11 59 10.3	19.58	0.2735
12 16 40.32	−11 58 25.4	22.95	0.2733	12 16 48.84	−11 58 30.7	21.90	0.1504
12 16 40.33	−12 02 01.4	21.41	0.7972	12 16 48.92	−12 01 23.8	22.36	0.7940*
12 16 40.35	−11 58 27.7	19.91	0.2739	12 16 48.93	−11 58 57.9	22.10	1.0742
12 16 40.70	−12 03 44.0	21.00	0.7930	12 16 48.96	−12 00 09.1	21.65	0.7863
12 16 40.91	−12 02 48.8	22.94	0.9480	12 16 49.03	−12 01 42.6	22.41	0.8000*
12 16 41.58	−11 58 46.4	22.93	0.8644	12 16 49.03	−12 01 53.1	22.01	0.7998
12 16 41.62	−11 59 30.8	21.94	1.0771	12 16 49.43	−11 59 16.5	22.38	0.4082
12 16 41.70	−12 03 05.4	21.36	0.8012	12 16 49.77	−12 01 35.8	21.87	0.7882
12 16 41.75	−12 00 44.9	21.66	0.7967	12 16 49.78	−11 58 34.4	23.02	0.7885
12 16 41.91	−12 02 44.0	22.10	0.8028	12 16 49.80	−12 01 39.2	21.21	0.7965
12 16 42.03	−12 01 50.9	20.62	0.7941	12 16 49.97	−12 01 10.6	21.46	0.6980*
12 16 42.26	−12 01 57.2	22.95	0.7950*	12 16 50.20	−12 00 03.8	22.17	0.6660
12 16 42.44	−12 02 34.8	20.65	0.2631	12 16 50.29	−11 59 59.4	22.95	0.7906
12 16 42.80	−12 03 39.5	21.33	0.7955	12 16 50.36	−12 00 12.0	22.57	0.9312
12 16 42.95	−11 59 53.6	22.01	0.7951	12 16 50.42	−12 00 48.0	21.92	0.7886
12 16 43.05	−11 59 36.5	22.18	0.2760	12 16 50.81	−11 57 57.6	21.18	0.6501
12 16 43.11	−11 58 11.3	22.50	1.0579	12 16 50.87	−12 02 05.7	20.93	0.7960*
12 16 43.18	−12 02 40.7	22.46	0.3194	12 16 51.36	−12 00 31.3	22.90	0.7841
12 16 43.18	−11 59 44.4	22.54	0.7948	12 16 51.57	−12 01 30.6	22.04	0.7220
12 16 43.37	−12 02 12.8	22.05	0.7839	12 16 52.20	−12 02 26.1	20.92	0.4062
12 16 43.53	−12 03 50.2	21.31	0.6693	12 16 52.21	−12 00 59.5	22.28	0.7882
12 16 43.76	−12 02 15.5	22.37	0.8028	12 16 52.33	−12 00 22.4	22.39	0.7583
12 16 43.77	−11 58 15.5	22.83	0.6558	12 16 52.65	−12 02 55.3	21.53	0.8263
12 16 43.78	−12 02 11.1	21.57	0.7913	12 16 53.08	−12 00 45.3	22.05	0.6490*
12 16 43.80	−12 00 53.6	21.10	0.7945	12 16 53.24	−12 01 36.2	21.74	0.7930*
12 16 43.87	−11 58 42.5	22.79	0.7956	12 16 53.28	−11 58 54.0	21.15	0.4763
12 16 43.92	−12 00 23.3	22.20	0.7831	12 16 53.39	−12 01 38.0	22.20	0.7925*
12 16 44.00	−11 57 51.6	21.92	0.7917	12 16 53.70	−11 59 27.6	22.18	0.2723
12 16 44.33	−12 01 38.4	21.72	0.7861	12 16 54.14	−11 57 55.9	22.49	0.8748
12 16 44.35	−12 01 42.9	21.05	0.7918	12 16 54.43	−12 01 32.9	22.48	0.7900*
12 16 44.47	−12 01 53.3	20.52	0.6703	12 16 54.76	−11 57 45.1	21.24	0.8746
12 16 44.51	−12 03 35.9	18.48	0.2344	12 16 54.81	−11 58 03.9	22.66	0.9827
12 16 44.53	−12 01 07.5	23.55	0.7934	12 16 54.96	−11 58 10.2	20.58	0.1034
12 16 44.59	−12 01 08.9	21.83	0.8001	12 16 55.26	−11 59 23.4	22.36	0.7950*
12 16 44.61	−12 02 35.8	21.93	0.6698	12 16 56.23	−11 59 39.1	22.92	0.8740*
12 16 44.67	−12 02 33.7	21.61	0.6708				